Spinel Formation for Stabilizing Simulated Nickel-Laden Sludge with Aluminum-Rich Ceramic Precursors

KAIMIN SHIH,[†] TIM WHITE,[‡] AND
JAMES O. LECKIE*,[†]

Department of Civil and Environmental Engineering, Stanford University, Stanford, California 94305-4020, and School of Materials Science and Engineering, Nanyang Technological University, Singapore 639798

The feasibility of stabilizing nickel-laden sludge from commonly available Al-rich ceramic precursors was investigated and accomplished with high nickel incorporation efficiency. To simulate the process, nickel oxide was mixed alternatively with γ-alumina, corundum, kaolinite, and mullite and was sintered from 800 to 1480 °C. The nickel aluminate spinel ($NiAl_2O_4$) was confirmed as the stabilization phase for nickel and crystallized with efficiencies greater than 90% for all precursors above 1250 °C and 3-h sintering. The nickel-incorporation reaction pathways with these precursors were identified, and the microstructure and spinel yield were investigated as a function of sintering temperature with fixed sintering time. This study has demonstrated a promising process for forming nickel spinel to stabilize nickel-laden sludge from a wide range of inexpensive ceramic precursors, which may provide an avenue for economically blending waste metal sludges via the building industry processes to reduce the environmental hazards of toxic metals. The correlation of product textures and nickel incorporation efficiencies through selection of different precursors also provides the option of tailoring property-specific products.

Introduction

It is well known that heavy metals are toxic and their discharge into receiving waters is detrimental to human health and the environment. Moreover, their elemental nature renders them more persistent in soils and aquifers than organic solvents and many other pollutants. When addressing heavy metal releases, a common strategy is to remove them from wastestreams by precipitation using processes that result in hazardous waste sludges. Among these toxic metals, nickel is a major component generated during electroplating operations. Electroless nickel plating plays an increasingly important role in manufacturing, especially for the fabrication of corrosion-resistant articles. Wastewaters generated by this type of operation can contain nickel concentrations of several thousand ppm or higher (*1−3*). In 1992, it was estimated that the electroless nickel plating industry produced more than 20 000 tons/year of waste in the U.S. alone (*4*) with a growth rate of 5% per year (*2*). The rapid increase of this type of wastewater is of worldwide concern and is receiving considerable attention.

At present, the majority of heavy metal-laden wastes are disposed of in controlled landfills. However, the high cost of this strategy, combined with the limited number of landfills capable of accepting highly toxic heavy metal wastes, has made the development of effective and economical treatment technologies essential. Many studies have successfully demonstrated the stabilization of radioactive waste in glass and ceramic materials by thermal treatment (*5−7*). An added advantage of such waste forms is the significant volume reduction achieved as compared to cementitious types (*8*), although the radioactive nature of these products means they are limited to containment in geologic repositories. Researchers have simulated nickel-laden sludge by using lime to precipitate nickel from its nitrate (*9, 10*) and chloride solutions (*11*), or directly via using nickel hydroxide (*12*). When thermally treated, these sludges decompose to nickel oxide (NiO), which is sufficiently soluble to be considered a waste compound requiring stabilization.

It has recently been found that nickel can be efficiently fixed in nickel aluminate spinel ($NiAl_2O_4$) by sintering nickel oxide with kaolinite (*13*), with immobilization taking place in two steps: (i) a low-temperature reaction between nickel oxide and a defect spinel, followed by (ii) a high-temperature reaction between nickel oxide and mullite. Kaolin, consisting chiefly of kaolinite ($Al_2Si_2O_5(OH)_4$), is a common clay type, and most ceramics are formed from high percentages of kaolinite (40−65%) (*14*). Kaolinite is readily available, and the FOB (free on board) price of kaolinite ranges from 4 to 8 cents per pound (*15*). A major byproduct of the U.S. industry is calcined kaolin generated by heating spray-dried and finely divided kaolin particles to render them anhydrous through transformation to mullite and silica (SiO_2). The price of calcined kaolin ranges from 15 to 25 cents per pound (*15*). In addition, aluminum oxides are inexpensive raw materials for $NiAl_2O_4$ formation as well.

The annual production of construction ceramics is of a volume sufficient to receive the ongoing generation of metal-laden sludge, even if incorporated in trace concentrations. The reasonably high firing temperatures normally used (900−1600 °C) in the brick, tile, and refractory aggregate industries may be helpful to promote an effective incorporation of waste materials into the ceramic matrix (*16−18*). To minimize the cost of waste blending, existing industrial production processes could be adapted to work within the limitations of precursor choice, sintering temperature, and sintering time. In this study, kaolinite, mullite ($3Al_2O_3 \cdot 2SiO_2$ from calcined kaolin), γ-alumina (γ-Al_2O_3), and corundum (α-Al_2O_3) were examined as possible Al-rich precursors.

$NiAl_2O_4$ formed by reactive sintering of nickel oxide and alumina (Al_2O_3) has been studied extensively. Philips et al. (*19*) compiled early data and published the first phase diagram of the NiO−Al_2O_3 system over the range of 1350−2100 °C to show the possibility of spinel formation above 1350 °C. Aluminum oxide has several common forms including α-alumina (α-Al_2O_3, a hexagonal crystalline structure also known as corundum), seven metastable Al_2O_3 phases (γ, δ, κ, ρ, η, θ, and χ), and several hydrated forms, such as aluminum trihydroxide (bayerite) and monohydroxide (boehmite) (*20−22*). To date, oxide sintering studies of $NiAl_2O_4$ have not emphasized the role of the alumina precursor (*23, 24*). Therefore, in this investigation, commercially available α-Al_2O_3 or γ-Al_2O_3 was chosen as the $NiAl_2O_4$ precursor. A reliable metal fixation strategy requires detailed analysis of immobilization mechanisms and efficiencies. In this study, the reaction pathways and feasibility of stabilizing nickel-laden sludge during the manufacture of construction ceram-

* Corresponding author phone: (650)723-2524; fax: (650)725-3164; e-mail: leckie@stanford.edu.
† Stanford University.
‡ Nanyang Technological University.

ics, such as bricks, tiles, and refractory aggregates, were investigated. Using readily available and inexpensive precursors, it was demonstrated that simulated Ni-laden sludge could be successfully immobilized with high incorporation efficiency by reactions with four Al-rich addictives.

Experimental Methods

Nickel incorporation efficiency experiments were conducted with samples prepared by firing nickel oxide with kaolinite, mullite, γ-alumina, or corundum. In most cases, the dwell time was fixed at 3 h for sintering temperatures ranging from 800 to 1480 °C. NiO powder (Fisher Scientific) gave an X-ray diffraction (XRD) crystallite size of 50−70 nm, and a surface area of 3.6 ± 0.5 m²/g after 300 °C heating and He-gas purging for 3 h to promote degassing. The surface area was measured via a Beckman Coulter SA3100 Surface Area and Pore Size Analyzer using the BET method. USP grade acid-washed kaolinite powder from Fisher Scientific yielded an XRD crystallite size of 5−10 nm and a BET surface area of 9.0 ± 2.9 m²/g. The measured BET surface area of kaolinite could be affected by the strong aggregation of fine kaolinite platelets, although all of the other powder raw materials are also in some degree of aggregation. The chemical composition for kaolinite was determined from a solution prepared by microwave-assisted acid digestion (U.S. EPA Method 3052) in which 0.5 g of kaolinite powder preheated at 700 °C for 12 h was mixed with 40 mL of aqua regia and 10 mL of hydrofluoric acid in a Teflon vessel and microwaved to total digestion. The digestion solution was diluted to 500 mL with MilliQ water, and the metal concentrations were derived from a TJA IRIS Advantage/1000 Radial ICP spectrometer with CLARITAS certified reference solutions (SPEX CertiPrep, Inc.). The chemical composition showed low impurity levels (<3% of several metal oxides), and its XRD pattern matched that of kaolinite (ICDD PDF#78-1996) as shown in the Supporting Information. The mullite precursor was prepared by calcining the kaolinite at 1300 °C for 24 h to yield mullite ($3Al_2O_3 \cdot 2SiO_2$; ICDD PDF #79-1455; XRD crystallite size of 5−20 nm) and cristobalite (SiO_2; ICDD PDF #76-0938), provided by the XRD pattern in the Supporting Information.

The γ-Al_2O_3 was prepared from HiQ-7223 alumina powder (Alcoa Corp.), which has a reported average particle size (d_{50}) of 54.8 μm. As received, HiQ-7223 alumina was confirmed by XRD to be boehmite (AlOOH; ICDD PDF #74-1895), which after heat treatment at 975 °C for 3 h was successfully converted to a γ-Al_2O_3 dominant material with an XRD crystallite size of 2−5 nm (20, 22). Further calcination at 1480 °C for 6 h transformed γ-Al_2O_3 to corundum (α-Al_2O_3; ICDD PDF#83-2080; XRD crystallite size of 10−20 nm), which was also used as a precursor for nickel stabilization. The XRD patterns of HiQ-7223 alumina and the thermally treated products are given in the Supporting Information.

NiO and the tailoring precursors were mixed by ball-milling in a water slurry for 22 h, molded into $2 \times 2 \times 2$ cm cubes, and dried at 95 °C for 3 days. These cubes were homogenized by mortar and pestle grinding, formed into 13 mm pellets at 125 MPa, and fired. After sintering, the pellets were air-quenched for the scanning electron microscopic (SEM) investigation and ground into randomly orientated powders for XRD analysis. The SEM investigation utilized an FEI XL30 Sirion SEM with FEG source, secondary electron detector for morphological information, backscattered electron detector for compositional information, and Si(Li) detector for energy dispersive spectroscopy (EDS). The powder samples were gold coated for the observation of particle morphology by the secondary electron imaging. After being polished with submicrometer diamond lapping film, pellets were coated with carbon. The secondary electron images were used to observe sample porosity, and the backscattered electron images were collected to identify compositionally distinct phases. Points and lines EDS analyses were also carried out as needed. In practice, construction ceramics will incorporate quite low levels of metal, so that product properties are not compromised. However, to investigate the incorporation mechanism in nickel-rich phases, the raw materials in this study were prepared with a Ni/Al mole ratio of 1:2, this being the stoichiometric maximum for nickel aluminate spinel.

Phase transformations during sintering were monitored by XRD. The diffraction patterns were collected using a Rigaku Geigerfex diffractometer (Rigaku Denki Co. Ltd.) equipped with a Cu X-ray tube operated at 35 kV and 15 mA, that had been calibrated using a quartz powder standard (ICDD PDF#33-1161). Scans were collected via a MDI XRD diffractometer control and data acquisition system (Material Data, Inc.) from 10° to 80° 2θ-angle, with a step size of 0.02° and a counting time of 1 s per step. Diffraction patterns were processed using JADE (version 6.5.3) developed by Material Data, Inc., with a whole pattern fitting (WPF) function using the Pawley method (25), to determine the weight percent of each crystalline phase. The background was processed with the polynomial function in the order of 3, and the weighted (R) and expected (E) reliability values were calculated using the following equations:

$$R\ (\%) = 100 \times \sqrt{\frac{\sum [w(i) \times (I(o,i) - I(c,i))^2]}{\sum [w(i) \times (I(o,i) - I(b,i))^2]}} \quad (1)$$

$$E\ (\%) = 100 \times \sqrt{\frac{(N - P)}{\sum I(o,i)}} \quad (2)$$

where $I(o,i)$ is the observed intensity of a fitted data point (i); $I(c,i)$ is the calculated intensity at this data point; $I(b,i)$ is the background intensity at this data point; $w(i)$ is the weight of this data point as $w(i) = 1/I(o,i)$; N is the number of fitted data points; P is the number of refined parameters; and $\sum I(o,i)$ in E is the sum of the overall fitted data points (N) that are 2σ above the fitted background.

The R/E ratio or "goodness of fit" will equal one in an ideal refinement, although, practically, the background and the peak profile mismatch lead to $R/E > 1$. To test the accuracy of this method, known percentages of NiO, corundum, and $NiAl_2O_4$ were subjected to WPF. The corundum used in this test was prepared by sintering γ-Al_2O_3 at 1480 °C for 6 h, while the $NiAl_2O_4$ was synthesized by combining NiO and γ-Al_2O_3 with a Ni/Al mole ratio of 1:2 at 1480 °C for 48 h. The results of this test with three independent replicates (Table 1) showed the maximum error in estimated phase weight percentages was about 3%. The random errors calculated by one-half of the data ranges (one-half of the difference between the maximum and the minimum values) were mostly below 2%, with the observed goodness of fit (R/E) generally around 1.5−2.0.

Results and Discussion

XRD confirmed that Ni was quantitatively incorporated in spinels using all four precursors. Figure 1 collates the XRD patterns of the 1250 °C-sintered samples and shows that $NiAl_2O_4$ is the predominant product. When NiO was transformed into $NiAl_2O_4$ with aluminum-rich precursors, a "transformation ratio (TR)" index was devised to indicate the nickel incorporation efficiency:

TABLE 1. Accuracy and Precision Tests of the Whole Pattern Fitting (WPF) Function Based on Three Independent Replicates[a]

	NiO, wt %	corundum, wt %	NiAl$_2$O$_4$, wt %	R, %	E, %	R/E
composition	0%	0%	100%			
WPF result	0.3 ± 0.4%	0.1 ± 0.1%	99.7 ± 0.5%	11.02 ± 0.10%	5.93 ± 0.01%	1.86 ± 0.02
composition	10%	10%	80%			
WPF result	8.7 ± 0.6%	9.3 ± 0.5%	82.0 ± 1.1%	11.56 ± 0.26%	6.77 ± 0.15%	1.71 ± 0.03
composition	20%	20%	60%			
WPF result	18.1 ± 1.1%	19.2 ± 0.5%	62.6 ± 1.4%	11.23 ± 0.16%	6.91 ± 0.07%	1.63 ± 0.02
composition	30%	30%	40%			
WPF result	27.7 ± 1.7%	29.6 ± 0.3%	43.0 ± 1.5%	10.79 ± 0.20%	6.77 ± 0.20%	1.59 ± 0.04
composition	40%	40%	20%			
WPF result	37.9 ± 1.8%	39.5 ± 0.4%	22.6 ± 1.4%	10.59 ± 0.08%	6.81 ± 0.14%	1.55 ± 0.02
composition	50%	50%	0%			
WPF result	48.3 ± 1.4%	49.8 ± 1.0%	1.7 ± 2.2%	10.59 ± 1.06%	6.24 ± 0.06%	1.70 ± 0.19

[a] Accuracy tested by known phase composition of NiO, corundum, and NiAl$_2$O$_4$ spinel powder mixtures. The weighted (R) and expected (E) values from whole pattern fitting (WPF) results were also obtained to monitor the goodness of fit (R/E).
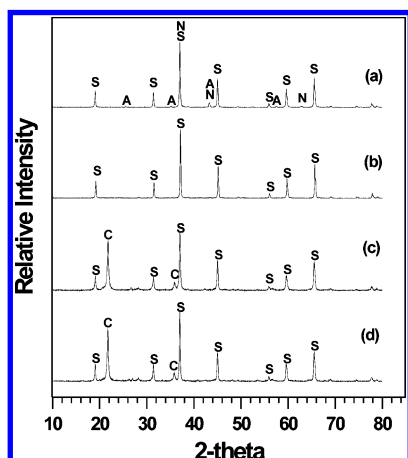
FIGURE 1. XRD results of 1250 °C and 3-h sintering with the precursor of (a) NiO + γ-Al$_2$O$_3$, (b) NiO + corundum, (c) NiO + kaolinite, and (d) NiO + mullite + cristobalite. "S" represents nickel aluminate spinel (NiAl$_2$O$_4$, ICDD PDF#78-0552); "N" is for nickel oxide (ICDD PDF#78-0429); "A" is for corundum (α-Al$_2$O$_3$; ICDD PDF#76-0938); and "C" is for cristobalite (SiO$_2$; ICDD PDF#76-0938).

transformation ratio (TR, %) =

$$\frac{\dfrac{\text{wt \% of NiAl}_2\text{O}_4}{\text{MW of NiAl}_2\text{O}_4}}{\left(\dfrac{\text{wt \% of NiAl}_2\text{O}_4}{\text{MW of NiAl}_2\text{O}_4} + \dfrac{\text{wt \% of NiO}}{\text{MW of NiO}}\right)} \quad (3)$$

where MW = molecular weight. For TR = 100%, complete transformation of nickel to NiAl$_2$O$_4$ was achieved; for TR = 0%, no nickel incorporation occurred. Taking the 1250 °C/3 h experiment as an example (Table 2), three independent replicates for each precursor showed high TR values (>90%) with goodness of fit (R/E) of 1.5–2.5. The larger R/E values of these samples, relative to the accuracy tests (Table 1), suggest peak fitting is more difficult in the mullite system as compared to corundum, due to the relatively weaker diffracted intensities and higher background.

NiAl$_2$O$_4$ Spinel Formation from γ-Al$_2$O$_3$ and α-Al$_2$O$_3$ Precursors. The γ-alumina (γ-Al$_2$O$_3$) phase is a low-temperature polymorph of corundum (α-Al$_2$O$_3$). Therefore, to investigate the crystallization of NiAl$_2$O$_4$ from γ-Al$_2$O$_3$, the maximum sintering temperature must be low enough to avoid premature transformation to corundum. After treatment at 990 °C for at least 3 h, γ-Al$_2$O$_3$ remained poorly crystalline without measurable transformation to the α-form. This result is consistent with the thermal treatment of boehmite, where possible metastable intermediates include cubic γ-Al$_2$O$_3$, tetragonal δ-Al$_2$O$_3$, and monoclinic θ-Al$_2$O$_3$ (20). From the

XRD pattern shown in the Supporting Information, the major phase in the 990 °C/3 h heated sample is γ-Al$_2$O$_3$, although δ and/or θ polymorphs are suggested by slight peak splitting at 2θ ≈ 45° and peak shoulder development at 2θ ≈ 31°.

When NiO and γ-Al$_2$O$_3$ were sintered together, NiAl$_2$O$_4$ was the main product together with residual reactants as provided by the XRD result in the Supporting Information. No reflections attributable to corundum (α-Al$_2$O$_3$) were observed at this low temperature and short sintering time. Nickel incorporation may proceed by two possible reaction pathways:

$$\text{NiO} + \gamma\text{-Al}_2\text{O}_3 \rightarrow \text{NiAl}_2\text{O}_4 \quad (4)$$

$$\text{NiO} + \alpha\text{-Al}_2\text{O}_3 \rightarrow \text{NiAl}_2\text{O}_4 \quad (5)$$

The transformation of γ-Al$_2$O$_3$ to the δ, θ, and α forms is gradual (dependent on time and temperature) (26), and to avoid this a rapid 1000 °C per hour temperature ramp was used. Figure 2 summarizes the transformation ratio of NiO + γ-Al$_2$O$_3$ and NiO + α-Al$_2$O$_3$ over the temperature range 800–1480 °C. Below 1100 °C, the presence of poorly crystalline transition alumina, which neither incorporated the nickel to form NiAl$_2$O$_4$, nor transformed into corundum, led to higher uncertainty in quantification. The crossover of the curves at ~1160 °C suggests that the NiO and γ-Al$_2$O$_3$ reaction (eq 4) was dominant at low temperatures, while the corundum precursor facilitates nickel incorporation at higher temperatures. The free energy of formation for γ-Al$_2$O$_3$ is higher than that for α-Al$_2$O$_3$ (21), from which it may be concluded that the reaction between NiO and γ-Al$_2$O$_3$ (eq 4) is favored energetically as compared to the reaction between NiO and α-Al$_2$O$_3$ (eq 5), and would explain the higher nickel incorporation efficiency with γ-Al$_2$O$_3$ at lower temperatures.

As the sintering temperature increased, the transformation rate of γ-Al$_2$O$_3$ to α-Al$_2$O$_3$ (k_2) will accelerate as shown in the Supporting Information. When the γ→α transformation rate (k_2) exceeds the spinel crystallization rate by γ-Al$_2$O$_3$ (k_1), the main NiAl$_2$O$_4$ formation mechanism is predominantly the reaction between α-Al$_2$O$_3$ and NiO (eq 5). Therefore, at high temperatures (i.e., >1160 °C, Figure 2), the chemical reactions for these two alumina precursors both involved α-Al$_2$O$_3$ (corundum) reacting with NiO, with physical mechanisms (e.g., grain size, shape, surface area) playing the key role in spinel development. Figure 3 shows the secondary electron images of the γ-Al$_2$O$_3$ and α-Al$_2$O$_3$ precursors and the distinct sample porosities that arise after reaction with NiO. The γ-Al$_2$O$_3$ occurred as solid aggregates (Figure 3a), but after sintering the resultant corundum was quite porous as crystal growth created voids with smooth subparticle surfaces (Figure

TABLE 2. Nickel Incorporation Efficiency Sintered at 1250 °C for 3 h[a]

precursor	NiO, wt %	spinel, wt %	TR, %	R, %	E, %	R/E
γ-type Al_2O_3	$3.7 \pm 0.3\%$	$92.1 \pm 0.4\%$	$91.3 \pm 0.6\%$	$13.73 \pm 2.86\%$	$6.97 \pm 0.24\%$	1.98 ± 0.48
corundum	$0.2 \pm 0.2\%$	$99.0 \pm 0.2\%$	$99.5 \pm 0.4\%$	$12.54 \pm 0.19\%$	$6.19 \pm 0.03\%$	2.03 ± 0.02
kaolinite	$0.9 \pm 0.2\%$	$58.9 \pm 2.5\%$	$96.4 \pm 0.6\%$	$20.51 \pm 0.21\%$	$8.47 \pm 0.16\%$	2.42 ± 0.06
mullite + cristobalite	$0.2 \pm 0.1\%$	$59.6 \pm 3.9\%$	$99.3 \pm 0.2\%$	$19.33 \pm 2.44\%$	$8.02 \pm 0.13\%$	2.41 ± 0.32

[a] Corresponding to the XRD patterns in Figure 1, the transformation ratio (TR) values were calculated by the estimated nickel oxide and spinel weight percentages to evaluate the incorporation efficiency. The weighted (R) and expected (E) values from whole pattern fitting (WPF) results were also obtained to monitor the goodness of fit (R/E).
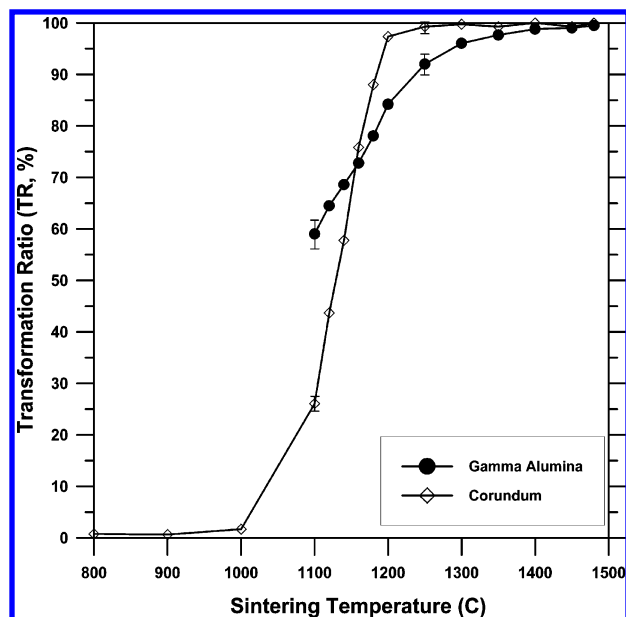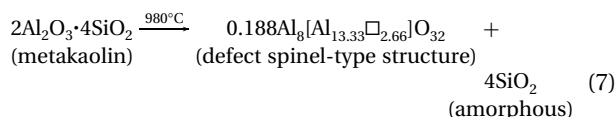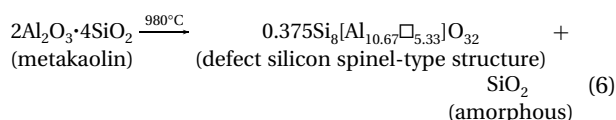

FIGURE 2. Nickel incorporation efficiency with γ-Al_2O_3 or corundum precursor. The values of transformation ratio (TR) were plotted for NiO + γ-Al_2O_3 samples and for NiO + corundum samples sintered at 800−1480 °C for 3 h. Below 1100 °C, the presence of poorly crystalline metastable alumina by γ-Al_2O_3 precursor leads to high uncertainty in the quantitative estimation.

3b). This is consistent with the quite significant density difference between γ-Al_2O_3 (3.657 g/cm³; ICDD PDF#79-1558) and corundum (3.983 g/cm³; ICDD PDF#83-2080). The different physical forms of the precursors lead to spinel with distinct microstructures. Figure 3c shows the 1480 °C and 3-h sintered product image from γ-Al_2O_3 precursor to be nearly composed of fully dense $NiAl_2O_4$ grains of ∼20 μm in diameter. A grain boundary is clearly visible, consistent with extensive lattice diffusion and grain growth. On the other hand, the product sintered with the same conditions but using the corundum precursor is more finely crystalline and contains numerous voids (Figure 3d). In this case, surface diffusion may be the dominant mass transfer mechanism as compared to lattice diffusion. It is reported that the growth of $NiAl_2O_4$ from nickel oxide and aluminum oxide was found to start from the interface between the two parent phases, and both Ni and Al ions counterdiffuse through the spinel lattice for growth to continue (27). Therefore, stronger surface diffusion may lead to a faster reaction rate, but smaller grains, and would be consistent with the higher nickel incorporation efficiency of corundum precursor samples sintered at high temperatures.

$NiAl_2O_4$ Spinel Formation from Kaolinite and Mullite Precursors. The phase transformation of kaolinite under thermal treatment has been extensively studied (28−31), the reaction sequence known leading to the kaolinite-to-mullite series. During this sintering process, physically bound water is removed at 110 °C, followed by decomposition of kaolinite with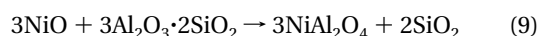 the loss of chemically bound water and transformation to amorphous metakaolin above 550 °C. Beyond 980 °C, the metakaolin is converted to a poorly crystalline defect spinel phase. At 1000 °C, mullite starts to form with excess amorphous silica crystallizing as cristobalite around 1300 °C, although Shih and Leckie (30) reported cristobalite crystallized at lower temperature when doped with nickel oxide. However, the kaolinite-to-mullite series is not completely understood, the most controversial point relating to the possible existence of a defect spinel phase (29). Prior work suggests that one of two reactions is operating:

$$2Al_2O_3 \cdot 4SiO_2 \xrightarrow{980°C} 0.375Si_8[Al_{10.67}\square_{5.33}]O_{32} +$$
$$\text{(metakaolin)} \quad \text{(defect silicon spinel-type structure)}$$
$$SiO_2 \quad (6)$$
$$\text{(amorphous)}$$

$$2Al_2O_3 \cdot 4SiO_2 \xrightarrow{980°C} 0.188Al_8[Al_{13.33}\square_{2.66}]O_{32} +$$
$$\text{(metakaolin)} \quad \text{(defect spinel-type structure)}$$
$$4SiO_2 \quad (7)$$
$$\text{(amorphous)}$$

where $\square$ = vacancy, and the defect spinel phase without silicon is identical to γ-Al_2O_3. Therefore, in the use of kaolinite as a precursor, nickel oxide may be reacting with spinel or mullite. In the former case, either γ-Al_2O_3 (same as eq 4) or the defect silicon spinel will be the reactant:

$$5.33NiO + Si_8Al_{10.67}O_{32} \rightarrow 5.33NiAl_2O_4 + 8SiO_2 \quad (8)$$
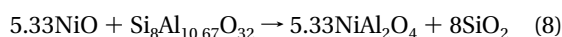
If mullite is involved, the reaction is:

$$3NiO + 3Al_2O_3 \cdot 2SiO_2 \rightarrow 3NiAl_2O_4 + 2SiO_2 \quad (9)$$

To investigate whether a spinel phase plays a role in the reaction with NiO, low temperatures are needed to avoid the formation of mullite. Therefore, the kaolinite precursor was sintered with nickel oxide at 990 °C for 7 days. XRD showed the only phase of sintered kaolinite to be poorly crystalline spinel (Figure 4a), but $NiAl_2O_4$ was observed in the final product (Figure 4b). The broad intensity between 15° and 30° was attributed to amorphous silica (SiO_2) (32, 33). Therefore, the defect spinel phase can be used to stabilize nickel, and either reaction pathway (eq 4 or eq 8) is possible. Because of the lack of diffraction reference data for defect silicon spinel, the pattern of Figure 4a was compared to the available γ-Al_2O_3 reference and found to be similar. However, this study does not address the true nature of the intermediate spinel phase generated during the kaolinite-to-mullite transformation, although the nickel incorporation ability of this compound is similar to that of γ-Al_2O_3.

To evaluate the nickel incorporation efficiency starting from different precursors, mixtures of NiO with kaolinite and calcined kaolinite were sintered from 800 to 1480 °C for 3 h. The 1300 °C and 24-h calcined kaolinite transformed to mullite and cristobalite (SiO_2). Under these conditions, silica does not react with nickel (13), and the only incorporation mechanism was through interaction between NiO and mullite as listed in eq 9. In sintering the mixtures of NiO and kaolinite, a WPF analysis that considered only NiO, $NiAl_2O_4$, mullite,
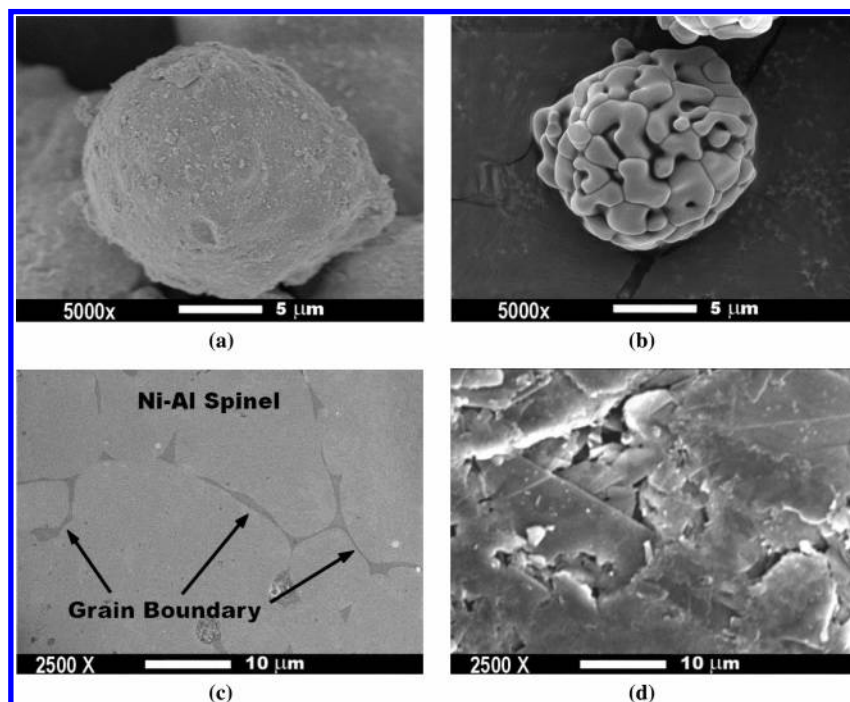
FIGURE 3. Secondary electron images of (a) γ-Al$_2$O$_3$ precursor particle; (b) corundum precursor particle; (c) polished surface of 1480 °C/3 h sintered product of NiO + γ-Al$_2$O$_3$; and (d) polished surface of 1480 °C/3 h sintered product of NiO + corundum. The grains in (c) were identified as nickel aluminate spinel (NiAl$_2$O$_4$), and the EDS data show the grain boundary may contain slightly more unreacted alumina or very minor Si as an impurity. Sample (d) showed porous texture even after polishing.
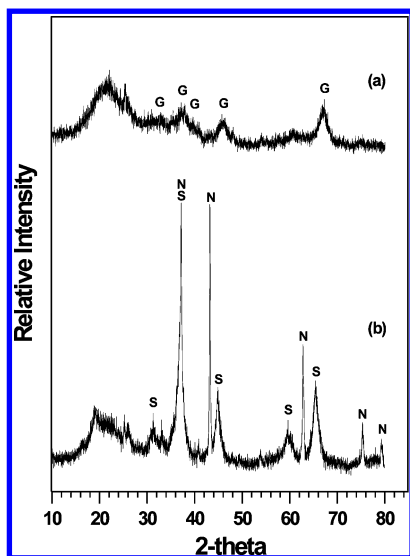
FIGURE 4. XRD results of (a) kaolinite precursor and (b) NiO + kaolinite sample sintered at 990 °C for 7 days. The result showed the defect spinel of kaolinite-to-mullite series reacted with NiO to form NiAl$_2$O$_4$. "N" represents nickel oxide (ICDD PDF#78-0429); "G" is for γ-alumina; and "S" is for nickel aluminate spinel (NiAl$_2$O$_4$, ICDD PDF#78-0552).
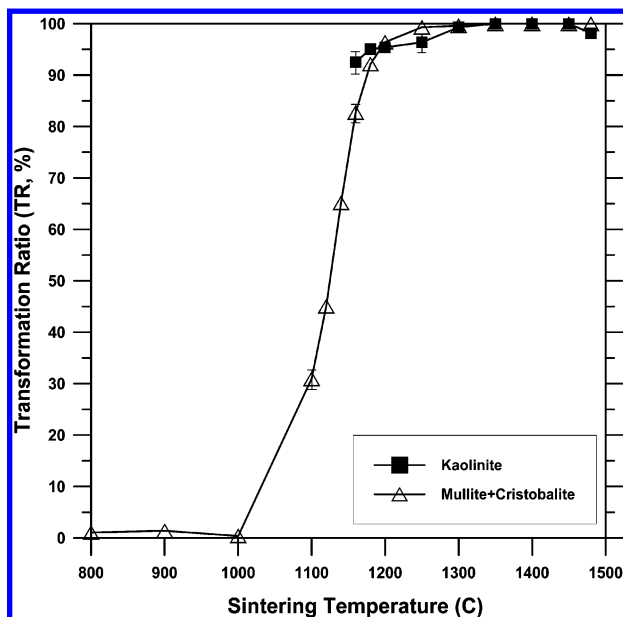

FIGURE 5. Nickel incorporation efficiency with kaolinite or mullite precursor. The values of transformation ratio (TR) were plotted for NiO + kaolinite samples and for NiO + mullite + cristobalite samples sintered at 800−1480 °C for 3 h. Below 1150 °C, quantification was not possible due to the presence of amorphous silica by kaolinite precursor.

and cristobalite showed the latter phase formed at ∼1150 °C, while below that temperature quantification was not possible due to the presence of amorphous silica. The transformation ratio of sintered samples from these two precursors indicated very high incorporation efficiency for nickel above 1200 °C (Figure 5). However, it is interesting to note the nickel incorporation efficiency decreased rapidly at temperatures <1200 °C. At 1160 °C, kaolinite displayed nickel incorporation efficiency 10% higher than mullite and may be the evidence for reaction between NiO and the defect spinel phase, while the mullite precursor reacted directly with NiO (eq 9). This is consistent with proven reactions between NiO and γ-Al$_2$O$_3$,

and between NiO and the defect spinel phase generated from the kaolinite-to-mullite series. Nevertheless, whether the reaction mechanism in eq 4 or eq 8 is dominant remains unresolved.

The nickel incorporation efficiencies of the kaolinite and mullite precursors are slightly higher than that of alumina precursors, because silica acted as a flux facilitating mass transfer during the solid-state reaction. After the formation of NiAl$_2$O$_4$, further sintering coarsens the grains and increases
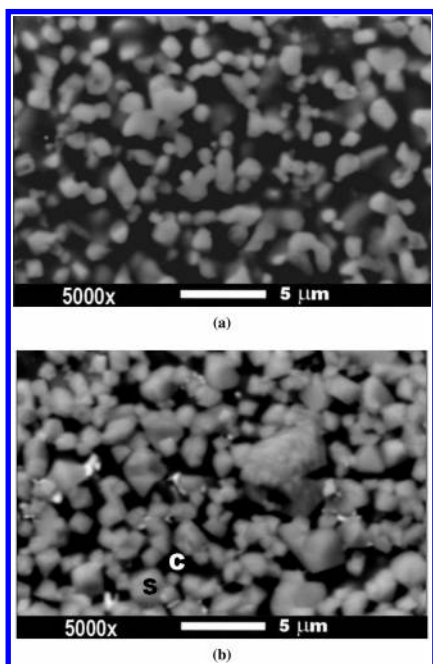
FIGURE 6. Backscatter electron images of polished surface of 1450 °C/3 h sintered (a) NiO + kaolinite sample and (b) NiO + mullite sample. The light-color grain (marked "S") showed the enrichment of Ni and Al (NiAl₂O₄); the darker matrix (marked "C") showed the enrichment of Si (cristobalite).

crystallinity. The microstructures of sintered products (1450 °C and 3-h) from both kaolinite and mullite precursors are compared in Figure 6, in which the sample derived from the mullite precursor showed greater mass transfer as evidenced by coarser $NiAl_2O_4$ crystals. The aluminum-rich ($NiAl_2O_4$) and the silicon-rich (cristobalite) areas were observed in both kaolinite + NiO and mullite + NiO samples and suggest the mullite precursor facilitates greater mass transfer at high temperatures that increases spinel crystallinity and product strength. This finding may guide the synthesis of making nickel-incorporated ceramics with acceptable mechanical properties. When waste metal sludges and natural ceramic raw materials are used, the presence of other components may affect the formation of $NiAl_2O_4$ by creating new reaction pathways. For example, Fe_2O_3 usually exists as an impurity in most clays and may form nickel ferrite spinel ($NiFe_2O_4$) with Ni-laden sludges (*34*). Alternatively, if the sludge is enriched with other divalent cations (Mg^{2+}, Zn^{2+}, Fe^{2+}, Mn^{2+}, etc.), the competition between Ni^{2+} and the other cations to form aluminate spinels may influence the nickel incorporation efficiency (*35*). The consideration of multi-spinel system may be worthy of future investigation to further understand the scientific basis of this promising strategy.

Acknowledgments

Supporting Information Available

One table and three figures showing the kaolinite composition, the XRD patterns of thermally treated HiQ-7223 alumina, the XRD patterns of the 990 °C sintered NiO and γ-Al_2O_3 mixture, and the diagram of $NiAl_2O_4$ formation rates from Al_2O_3 precursors. This material is available free of charge via the Internet at http://pubs.acs.org.

Literature Cited

(1) Ying, W. C.; Bonk, R. R.; Tucker, M. E. Precipitation treatment of spent electroless nickel plating baths. *J. Hazard. Mater.* **1988**, *18*, 69−89.

(2) Bolger, P. T.; Szlag, D. C. Investigation into the rejuvenation of spent electroless nickel baths by electrodialysis. *Environ. Sci. Technol.* **2002**, *36*, 2273−2278.

(3) Chang, P.-H.; Huang, Y.-H.; Hsueh, C.-L.; Lu, M.-C.; Huang, G.-H. Treatment of nonbiodegradable wastewater by Electro-Fenton method. *Water Sci. Technol.* **2004**, *49*, 213−218.

(4) Anderson, R. W.; Neff, W. A. Electroless nickel bath recovery by cation-exchange and precipitation. *Plat. Surf. Finish.* **1992**, *79*, 18−26.

(5) Lewis, M. A.; Fischer, D. F.; Smith, L. J. Salt-occluded zeolite as an immobilization matrix for chloride waste salt. *J. Am. Ceram. Soc.* **1993**, *76*, 2826−2832.

(6) Lewis, M. A.; Fischer, D. F.; Murphy, C. D. Properties of glass-bonded zeolite monlith. *Ceram. Trans.* **1994**, *45*, 277−286.

(7) Wronkiewicz, D. J.; Bates, J. K.; Buck, E. C.; Hoh, J. C.; Emery, J. W.; Wang, L. M. Radiation Effects in Moist-air Systems and the Influence of Radiolytic Product Formation on Nuclear Waste Glass Corrosion. Argonne National Laboratory Report No. ANL-97/15; Argonne National Laboratory: Argonne, IL, 1997.

(8) Bostick, W. D.; Hermes, W. H. Control of regulated metals at DOE Oak Ridge reservation sites. *Waste Manage.* **1993**, *13*, 439−454.

(9) Roy, A.; Eaton, H. C.; Cartledge, F. K.; Tittlebaum, M. E. Solification/stabilization of a heavy metal sludge by a portland cement/fly ash binding mixture. *Hazard. Waste Hazard. Mater.* **1991**, *8*, 33−41.

(10) Bricka, R. M.; Jones, L. W. An Evaluation of Factors Affecting the Stabilization/Solidification of Heavy Metal Sludge. EPA/600/S-92/023, USEPA, 1992.

(11) Andres, A.; Ibanez, R.; Ortiz, I.; Irabien, J. A. Experimental study of the waste binder anhydrite in the solidification/stabilization process of heavy metal sludges. *J. Hazard. Mater.* **1998**, *57*, 155−168.

(12) Diet, J.-N.; Moszkowicz, P.; Sorrentino, D. Behaviour of ordinary portland cement during the stabilization/solidification of synthetic heavy metal sludge: Macroscopic and microscopic aspects. *Waste Manage.* **1998**, *18*, 17−24.

(13) Shih, K.; White, T.; Leckie, J. O. Sintering of simulated Ni-bearing sludge and kaolinite: Ni−Al spinel formation. Proceedings, Joint Clean Water Programme Symposium; Singapore, 2005.

(14) Velde, B. *Introduction to Clay Minerals*; Chapman & Hall: London, UK, 1992.

(15) Murray, H. *Industrial Clays Cases Study*; International Institute for Environment and Development: England, 2002.

(16) Martelon, E.; Jarrige, J.; Ribeiro, M. J.; Ferreira, J. M.; Labrincha, J. A. New clay-based ceramic formulations containing different solid wastes. *Ind. Ceram.* **2000**, *20*, 71−76.

(17) Wiebusch, B.; Seyfried, C. F. Utilization of sewage sludge ashes in the brick and tile industry. *Water Sci. Technol.* **1997**, *36*, 251−258.

(18) Resende, W. S.; Stoll, R. M.; Pallone, E. M. J. A.; Chuha, F. N.; Bradt, R. C. Spinel refractory aggregates from natural raw materials. *Miner. Metall. Process.* **2001**, *18*, 68−74.

(19) Phillips, B.; Hutta, J. J.; Warsaw, I. Phase equilibria in the system NiO−Al₂O₃−SiO₂. *J. Am. Ceram. Soc.* **1963**, *46*, 579−583.

(20) Zhou, R.-S.; Snyder, R. L. Structures and transformation mechanisms of η, γ and θ transition aluminas. *Acta Crystallogr., Sect. B* **1991**, *47*, 617−630.

(21) Wolverton, C.; Hass, K. C. Phase stability and structure of spinel-based transition aluminas. *Phys. Rev. B* **2000**, *63*, 024102.

(22) Wang, Y.; Suryanarayana, C.; An, L. Phase transformation in nanometer-sized γ-alumina by mechanical milling. *J. Am. Ceram. Soc.* **2005**, *88*, 780−783.

(23) Mocala, K.; Navrotsky, A. Structure and thermodynamic variation in nickel aluminate spinel. *J. Am. Ceram. Soc.* **1989**, *72*, 826−832.

(24) Roelofsen, J. N.; Peterson, R. C.; Raudsepp, M. Structure variation in nickel aluminate spinel (NiAl₂O₄). *Am. Mineral.* **1992**, *77*, 522−528.

(25) Pawley, G. S. Unit-cell refinement from powder diffraction scans. *J. Appl. Crystallogr.* **1981**, *14*, 357−361.

(26) Kao, H. C.; Wei, W. J.; Huang, C. Y. Two-stage densification of ultrafine trasition alumina seeded with α-phase particulates. *J. Ceram. Process. Res.* **2003**, *4*, 34−41.

(27) Schmalzried, H. *Chemical Kinetics of Solids*; Weinheim: New York, 1995.

(28) Brindley, G. W.; Nakahira, M. The kaolinite-mullite reaction series: I, A survey of outstanding problems. *J. Am. Ceram. Soc.* **1959**, *42*, 311−314.

(29) Schneider, H.; Okada, K.; Pask, J. A. *Mullite and Mullite Ceramics*; John Wiley and Sons: New York, 1994.

(30) Shih, K.; Leckie, J. O. Stabilizing simulated Ni-bearing sludge by aluminum-rich and iron-rich ceramic precursor. Proceedings, Joint Clean Water Programme Symposium; Singapore, 2005.

(31) Chen, C.-Y.; Tuan, W.-H. Evolution of mullite texture on firing tape-caste kaolin nodies. *J. Am. Ceram. Soc.* **2002**, *85*, 1121−1126.

(32) MacKenzie, K. J. D.; Hartman, J. S.; Okada, K. MAS NMR evidence for the presence of silicon in the alumina spinel from thermally transformed kaolinite. *J. Am. Ceram. Soc.* **1996**, *79*, 2980−2982.

(33) McConville, C. J.; Lee, W. E.; Sharp, J. H. Microstructural evolution in fired kaolinite. *Br. Ceram. Trans.* **1998**, *97*, 162−168.

(34) Stegemann, J. A.; Roy, A.; Caldwell, R. J.; Schilling, P.; Tittsworth, R. Understanding environmental leachability of electric arc furnace dust. *J. Environ. Eng.* **2000**, *126*, 112−120.

(35) Deer, W. A.; Howie, R. A.; Zussman, J. *An Introduction to the Rock-Forming Minerals*; John Wiley and Sons: New York, 1992.